
Article:
Chen, H. and Qin, N. orcid.org/0000-0002-6437-9027 (2017) Trailing-edge flow control for wind turbine performance and load control. Renewable Energy, 105. pp. 419-435. ISSN 0960-1481

https://doi.org/10.1016/j.renene.2016.12.073

Trailing-edge Flow Control for Wind Turbine Performance and Load Control

Hao Chen and Ning Qin

Department of Mechanical Engineering, the University of Sheffield, Mappin Street, Sheffield, S1 3JD, UK

Highlights

- Flow around 3D turbine blade is dominated by spanwise flow on the suction side at higher wind speeds for stall regulated wind turbine.
- Flow control effects from 2D sectional studies cannot be realized for 3D rotating blade due to suction side spanwise flow.
- To improve wind turbine off-design performance, the micro jet performs better at lower wind and the micro tab at higher wind conditions.
- At high wind speeds, unsteady simulations give a much better comparison with the wind tunnel test data for the mean torque generated.

Trailing-edge Flow Control Devices for Wind Turbine Performance and Load Control

Hao Chen and Ning Qin

Department of Mechanical Engineering, the University of Sheffield, Mappin Street, Sheffield, S1 3JD, UK

Abstract

This paper reports an investigation into the performance of trailing-edge flow control devices on horizontal axis wind turbines by solving the three dimensional Reynolds averaged Navier-Stokes equations in the rotational framework. The validation case selected for this work is the NREL Phase VI blade with wind tunnel experimental data. The trailing-edge flow control devices studied include microtabs and microjets installed near the trailing-edge of the rotating blade. The divergent trailing-edge is also included in the study as a passive flow control device due to its practical interest. These trailing-edge devices are implemented on the fixed-pitch NREL Phase VI blade, using the original performance and flow characteristics as a benchmark. Both 2D and 3D simulations are carried out in order to investigate the suitability of the 2D blade sectional design analysis and control for the actual 3D rotating blades.

Keywords: flow control, microtabs, microjets, divergent trailing-edges, efficiency, load control.

Introduction

Improving the aerodynamic performance of the wind turbine blade is one of the most significant factors to maximize the efficiency of converting wind kinetic energy into mechanical then electrical energy. Great progress has been made in the recent years in blade aerodynamic design and a modern horizontal axis wind turbine (HAWT) can reach a relatively high power coefficient. However most present HAWTs are designed for a rated power at a specified wind speed. Beyond this wind speed range the efficiency of the wind turbine can drop significantly. Considering the manufacturing difficulties of an adaptive/morphing turbine blade to suit different wind conditions, flow control can offer improved wind turbine performance for a wider range of wind speed around the rated condition.

Hansen and Madsen (2011) reviewed both passive and active flow control devices for wind turbines, including flaps/deformable trailing edge, microtabs, morphing, active twist, suction/blowing, synthetic jets, active vortex generators (VGs) and plasma actuators. The present study investigates two typical flow control devices, microtabs and microjets, along with the divergent trailing edge (DTE) aerofoil concept proposed by Henne and Gregg (1991) for comparing their effectiveness on 3D wind turbine blade in a rotating frame. The following literature review covers some previous studies for microtabs, microjets and DTE to put the present research in context.

Using microtab for wind turbine load control was derived from the Gurney flaps concept for aircraft wings. The Gurney flap was first proposed by an automobile racer Dan Gurney and his idea was later exploited by Liebeck (1978) for aircraft wing aerofoil applications. Theoretically the Gurney flap increases the lift coefficient (C_L), including the maximum $C_{L,}$ at a range of angles of attack (AOAs) of the aerofoil when it is deployed on the pressure side of the aerofoil at the trailing edge. However it also induces higher drag coefficient (C_D) and therefore the lift to drag ratio needs to be considered carefully when such concept is applied in the aircraft design.

Unlike aircraft, the main driving force of HAWTs is the lift force and the drag force is much less important in the design process. Therefore the GF concept is significant for load improvement or control of HAWTs. An active flow control device some space is required inside the aerofoil for actuation purpose. Von Dam *et al.* (2001) first proposed the concept of microtab which was deployed from 0% to 10% chord position from the trailing edge of the aerofoil. This study carried out both 2D computational research and experiments on the GU-25-5(11)-8 aerofoil. The results showed that a 1% chord height (3mm) solid microtab at 95%c position increased the C_L by up to 50% at 0^o AOA. Another important conclusion from this study is that for the aerofoil the closer the microtab deployed to the trailing edge the more C_L increases. Zayas *et al.* (2006) showed that microtab on the suction side as an active device cannot only be beneficial for load alleviation but also improve the energy generation if installed on the pressure surface.

Van Dam *et al.* (2007) investigated the microtab and active micro-flap around the trailing-edge, in order to reduce the aerodynamic-fatigue loads on wind turbine blades. The results showed that deploying the microtab at around 1% chord length from the trailing-edge or moving trailing-edge flaps with around 10% chord length can effectively mitigate high frequency loads of the blade. Again, this study is limited to the 2D analysis without considering the complicated 3D interaction due to the flow control devices. Cooperman (2013) tested the microtabs and microjets on a fixed S809 aerofoil blade in a wind tunnel and the results showed that deploying a 1% chord length microtab near the x/C = 90% position of the aerofoil produced a ΔC_l of 0.18.

Microjet is similar to microtab in increasing the lift force when deployed near the trailing edge on the pressure side or reducing the lift force when deployed on the suction side. Braylock et al. (2013) studied microjets and microtabs on the NACA0012 aerofoil. Their results showed that both the response time and changes to the C_L of the NACA0012 aerofoil from these two types of flow control devices are similar except for that the microjet had around 30% lower drag compared to that from the microtab. Their further study (Cooperman *et al.* 2014) also showed that using microtab and microjet can reduce the lift force variation when wind speed changes, which can effectively protect the HAWT in gust situation.

With the larger and larger size of modern HAWTs, the flapwise root bending moment of the blade should be considered carefully for structural issues for wind turbines. Hurley et al. (2016) simulated the trailing edge microjet effects on the 5MW NREL (national renewable energy laboratory) reference blade based on 2D data. Results showed that deploying a 14 meters microjet from 30-meter span to 44-meter span position of the blade can effectively reduce the flapwise root bending moment of the blade by 3.5%-28% at different wind speeds.

The divergent trailing-edge is a concept by Henne and Gregg (1991) for aircraft wings, which is proved to be beneficial for high Cl/Cd of supercritical aerofoils (Li et al., 2007). This concept was applied with a large scale divergent trailing-edge at 3% chord length for its performance on the wind turbine field. Baker *et al.* (2006) investigated into the blunt trailing-edge wind turbine 35%c thick aerofoil both experimentally and numerically at a 2D condition. The experimental

results showed that by increasing the thickness of the trailing-edge, the maximum L/D can be increased from 35.5 to 44 at the Re = 666,000 flow condition for the 8.75%c trailing-edge thickness redesigned aerofoil and the maximum C_l can be increased from 1.5 to 2.16 for the 17.5%c thickness trailing-edge redesigned aerofoil. This study also showed that increasing the thickness of trailing-edge is able to effectively improve the lift force of the aerofoil at the 2D condition.

In summary, all previous studies mentioned above show some progresses in understanding the trailing edge devices on HAWT blades. However, these studies on trailing edge devices are based on the study of the 2D blade sections, which does not fully reflect the flow physics for the wind turbine environment in the 3D rotating framework. mThe validity of some of the conclusions drawn from the 2D studies regarding the effectiveness of the trailing edge flow control is questionable when there is strong spanwise flow along the blade. This study aims to fill the gap and investigate the effectiveness of trailing edge flow control devices in the context of 3D rotating framework at and away from the rated conditions and to compare it with the same devices from the 2D blade sectional study. The devices include two typical trailing edge flow control devices (microtab and microjet) along with the concept of divergent trailing edge of HAWTs.

Validation study on the NREL Phase VI wind turbine

The NREL Phase VI wind turbine is a typical rotor with extensive experimental data (Schrech *et al.*, 2001) and, therefore, it was selected to be a validation case in this study. The wind tunnel test was conducted in the NASA Ames low speed wind tunnel with a test cross section of 24.4m x 36.6m at different speeds.

Geometry and Mesh Generation

The geometry model of NREL Phase VI two blade wind turbine is generated using ICEM mesh generator. Table 1 shows the basic description of the blade details. The computational domain is confined to embody one of the blades in a semi-cylindrical domain using symmetrical boundary conditions. Because there is no detailed description for the blade tip of NREL Phase VI turbine from published data, a flat tip shape is assumed in this project. Figure 1 shows the cross-sectional aerofoil of the NREL Phase VI blade and the whole blade shape.

A fully structured multi-block mesh is used for this study. ANSYS Fluent CFD package is used for solving the Reynolds averaged Navier-Stokes equations. The two-equation k-ω SST model is used for the turbulence closure, where the wall y^+ needs to be around 1 for accuracy to resolve the turbulent boundary layer. Therefore the mesh needs to be very fine near the blade surface in the wall normal direction, leading to a first cell height around 0.01 mm near the blade tip. The total elements of the medium mesh for the problem are around 2 million. An O-type mesh topology is used around the wind turbine and the mesh quality is controlled so as the determinant of Jacobian matrix (quality criterion for hexahedral elements in ICEM) and the Eriksson skewness are above 0.3.

Table 1. Basic description of NREL Phase VI blade

Number of blades	**2**	**Tip pitch angle**	**3 degrees**
Rotor diameter	10.06m	**Blade profile**	S809
Angular velocity	7.54rad/s	**Blade chord length**	0.358m-0.728m (Linearly tapered)
Blade thickness	t/c = 20.95%	**Twist angle**	Non-liner twist along the span

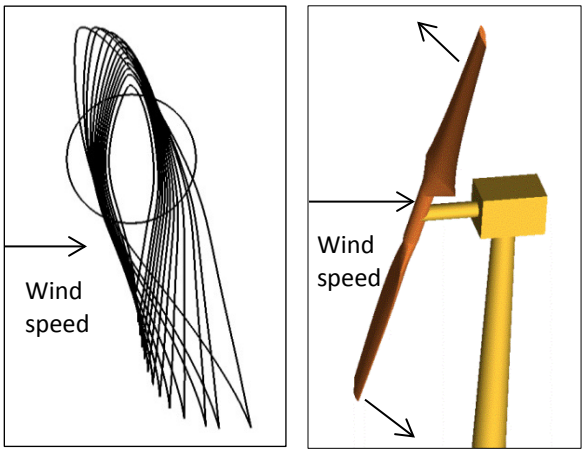

Figure 1. Left: Cross section of the aerofoils of the blade; right: the whole blade

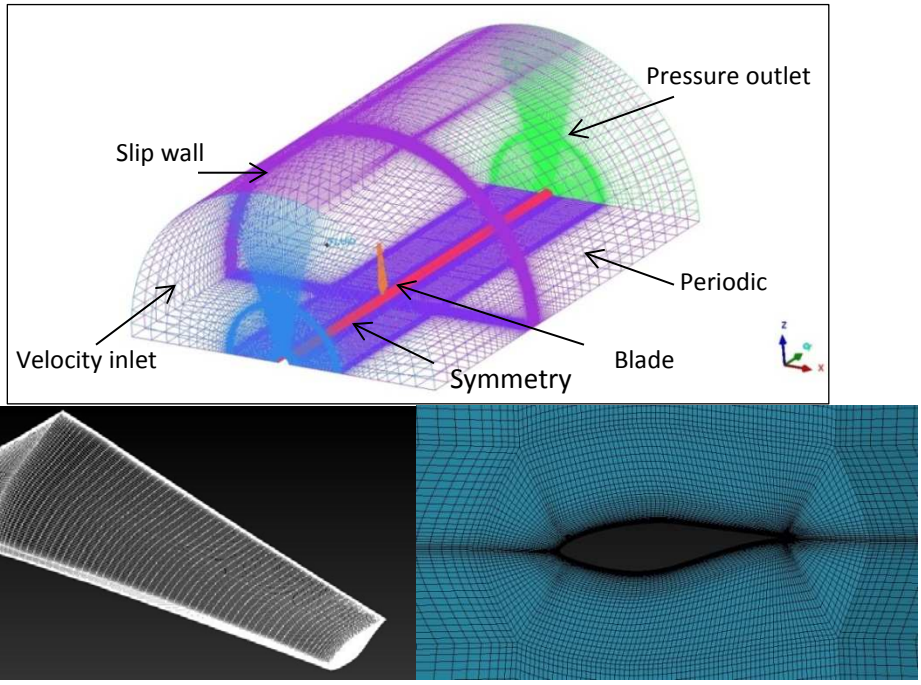

Figure 2. Top: Mesh overview of the whole domain; bottom: blade surface and cross section mesh.

CFD solution setup

The detailed boundary conditions of this study are shown in Table 2 and Figure 2. In this case, the rotating frame is used and the rotating speed of the blade is set at a constant angular speed of 7.54 rad/s. The turbulence intensity and length scale are set to be 0.1% (according to the wind tunnel condition) and 0.02m respectively. The outer boundary is chosen to be at 12.2m from the axis of rotation, to match the wind tunnel wall-to-wall distance in the vertical direction. A slip boundary condition (no through flow) is applied at the outer boundary.

In this project the coupled algorithm and the Green-Gauss Node based discretization scheme are applied. The simulations were set to be steady flow condition when wind speed is below 10m/s. However when the wind speed is higher than 13m/s, the blade exhibits large scale separation and the flow is no longer steady. Therefore unsteady simulations were carried out for 13m/s and 15m/s wind speed. In these cases, the time-step size was set to be 0.0006s with 20 sub-iterations per time-step. Simulations were run on a university HPC system ICEBERG. In the numerical study, the wind speed U is set varying from 5m/s to 15m/s. The rotational speed of the wind turbine is 7.54 rad/s, leading to the tip speed ratios (TSR) from 2.78 to 7.6 for the different wind speeds.

Table 2. Boundary conditions setting.

Parts	Boundary condition
Blade	No-slip wall
Outer boundary	Slip wall
Inlet	Velocity-inlet
Periodic Faces	Periodic
Outlet	Pressure-outlet
Inner boundary	Slip

Results

In this part, the aerodynamic forces are analysed in the context for wind turbine energy extraction. This is achieved by integrating the pressure and skin friction forces and correspondingly the moment on the blade and projecting them in the direction of rotation. Pressure distributions and streamlines near the blade are also analysed. The comparison of the pressure coefficient distribution with the experimental data is presented. In this study two radial positions are selected for analysis at r/R= 0.47 and 0.8, respectively.

The mesh sensitivity study is a very important part in numerical simulations. In this study, three mesh sizes are tested, at 1 million, 2 million and 4 million, respectively, at the wind speed of 7m/s. The computed torques of the blade is shown in Table 3. According to the table it can be seen that the computed torque shows some small variation with the changes in the three cases. The computational torque at 4 million cells gives a closer comparison with the experimental

value (780 Nm), and the comparison is reasonably good. Due to the availability of the computational resource, the 4 million cell mesh is used in the following study without further refining the mesh.

Table 3. Simulated torques of different meshes (U = 7m/s).

Mesh sizes	Torque (Nm)
1 million grids	814
2 million grids	809
4 million grids	796

The torque of the single simulated wind turbine blade can be extracted from the CFD solver directly. Both steady simulations and unsteady simulations are carried out to see the differences compared to the experimental data. Figure 3 shows that in all wind speeds the unsteady flow computation predict the wind turbine performance reasonably well using the k-ω SST model. The biggest discrepancy here is at the 10m/s wind speed condition, which is with a 6.52% over-prediction of the torque.

Table 4. Torque difference between CFD and experimental data

Wind speed	Experimental torque (Nm)	CFD torque Nm (Steady cases)	%difference	CFD torque Nm (Unsteady cases)	%difference
5 m/s	310	315	1.6%	317	2.26%
7 m/s	780	796	2.1%	801	2.69%
10 m/s	1366	1448	6%	1455	6.52%
13 m/s	1215	1096	9.8%	1221	0.49%
15 m/s	1183	902	23.8%	1174	0.76%

Table 4 shows the results from both steady and unsteady RANS computations. It can be see that for cases at 5m/s, 7m/s and 10m/s wind speeds both the steady and unsteady simulations can accurately predict the aerodynamic torque of the wind turbine within less than 7% error differences. However for 13m/s and 15m/s wind speeds the steady simulations show much larger errors than that from the unsteady cases which are as high as 23.8% differences at the 15m/s wind speed case. For the given rotational speed of the wind turbine, a higher wind speed implies a higher angle of attack of the relative flow to the turbine blade section. For 13 m/s and 15 m/s wind speeds, large flow separation occurs, inducing unsteady flow around the blade. This indicates that the steady flow assumption is no longer valid, resulting in erroneous torque

prediction. However, when unsteady RANS is solved, the average torques predicted are in much better comparison with the experimental data at the two higher wind speed conditions, as shown in Table 4 and Figure 3.

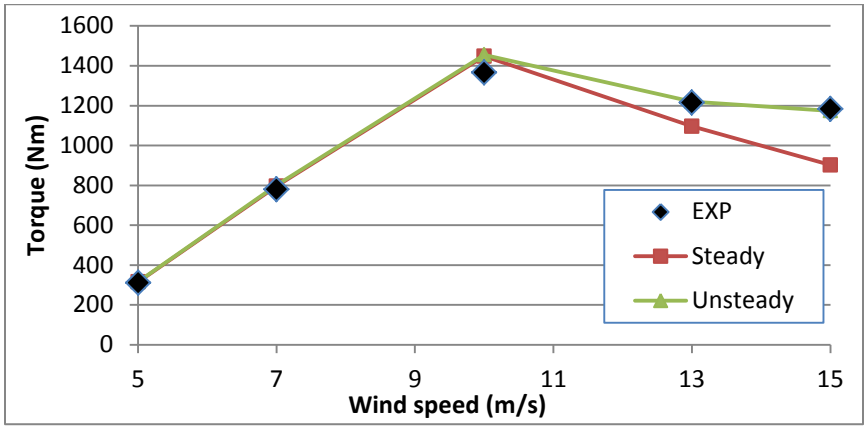

Figure 3. Torque comparison between CFD (steady and unsteady) and experimental data

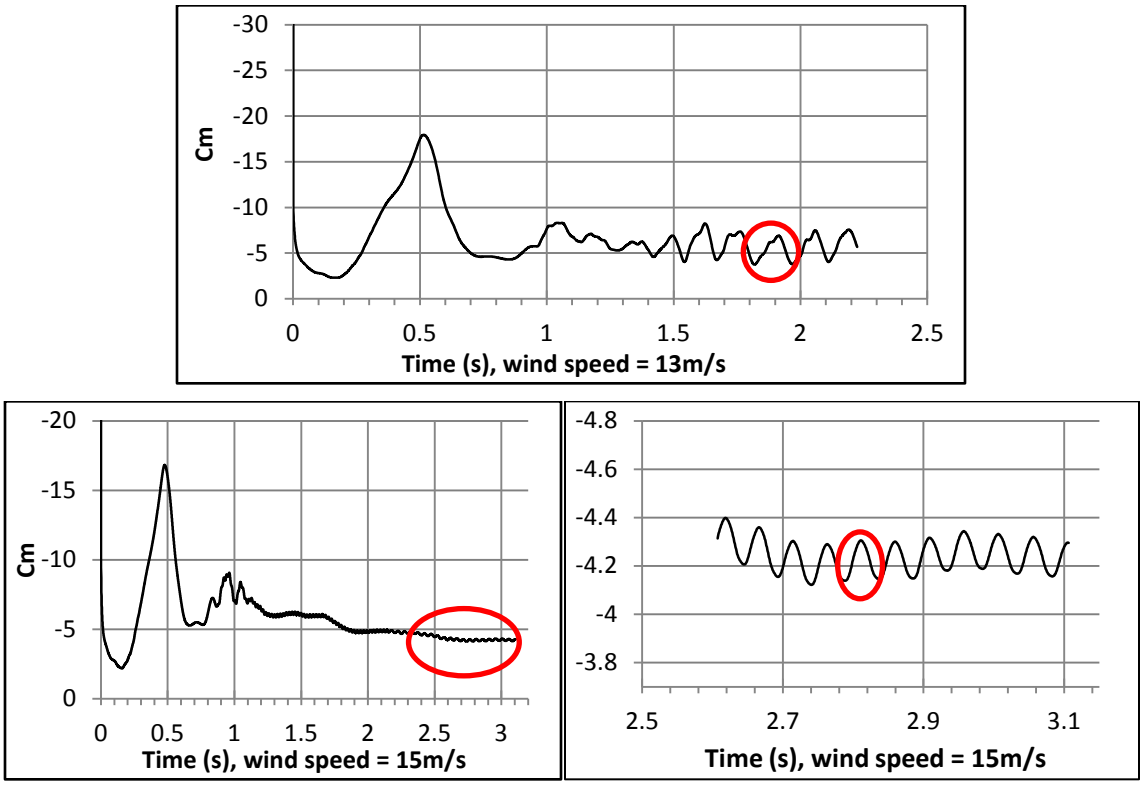

Figure 4. C_m convergence history for the original wind turbine at 13m/s and 15m/s wind speed, the final mean torque is calculated at one cycle as shown in the graph.

The C_m converge history of the steady cases at higher wind speeds is waving up and down in a 20% difference. In this situation the torque is calculate as the mean torque value. For the

unsteady simulations at higher wind speed cases, which are shown in Figure 4, the flow became periodic due to vortex shedding captured in the computational simulation. The torques for the unsteady cases is obtained averaging the last cycle of the momentum coefficient from the convergence history. In the later part the instantaneous case which is closest to the mean torque is selected for flow condition and pressure coefficient analysis. Therefore considering the computational accuracy and time, the 5m/s, 7m/s and 10m/s wind speed cases will be run in steady flow condition and the 13m/s and 15m/s wind speed cases will be run in unsteady flow condition in further study on the flow control devices.

The pressure coefficient of the cross-sections of the blade is also compared. Here as figure 5 shows, for most cases the simulation can correctly predict the pressure coefficients compared to the experimental data. It is also noted that at 10 m/s, the CFD result over-predict the cross-sectional force at r/R = 0.47 spanwise section. This discrepancy has also been observed in some previously published works such as the studies from Mahu and Popescu (2011) and Mo and Lee (2012). This may be attributed to the difficulty of the employed turbulence model, the k-ω SST model or the steady RANS approach in capture the flow separation at this location for this speed condition. Nevertheless the separation regions (pressure plateau) at the other speeds or locations have been captured reasonably well as shown in the figure.

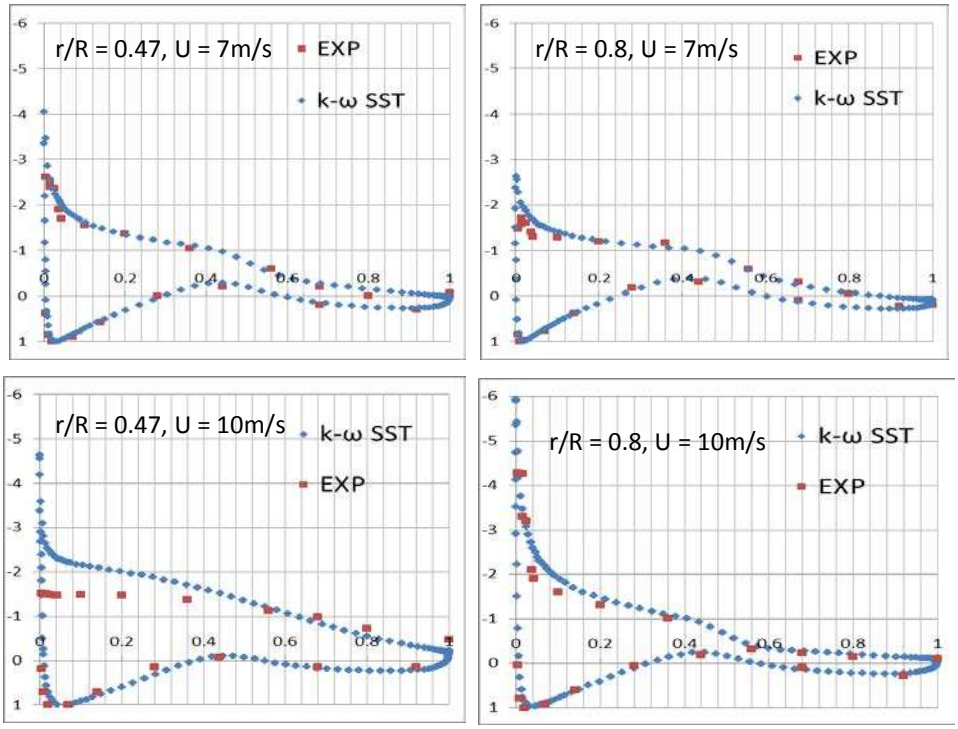

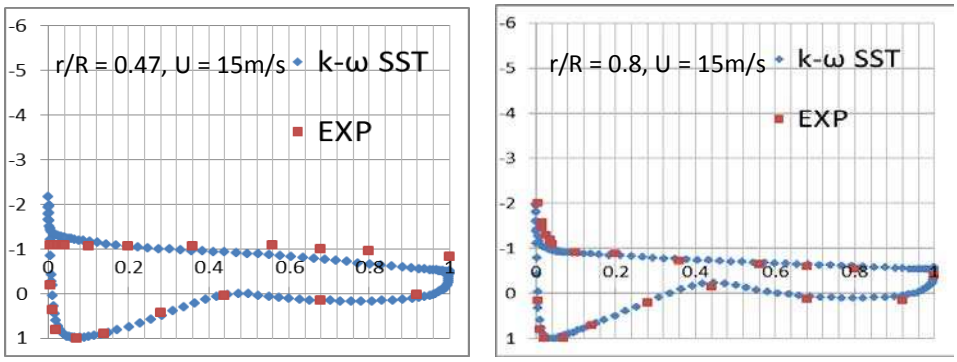

Figure 5. Pressure coefficient comparison at r/R = 0.47 and 0.8 span positions. Top: wind speed = 7 m/s; middle: wind speed = 10 m/s; bottom: wind speed = 15 m/s (t = 3.12s)

Figure 6 shows the velocity streamlines at r/R = 0.47 and 0.8 positions in different wind speeds. When the wind speed is 7m/s the flow around the blade is almost fully attached and when wind speed is higher than 10m/s the flow at the suction side of the blade begins to be detached. When wind speed reaches 15m/s the blade is stalled even at the r/R = 0.8 position with large flow separation at the suction side.

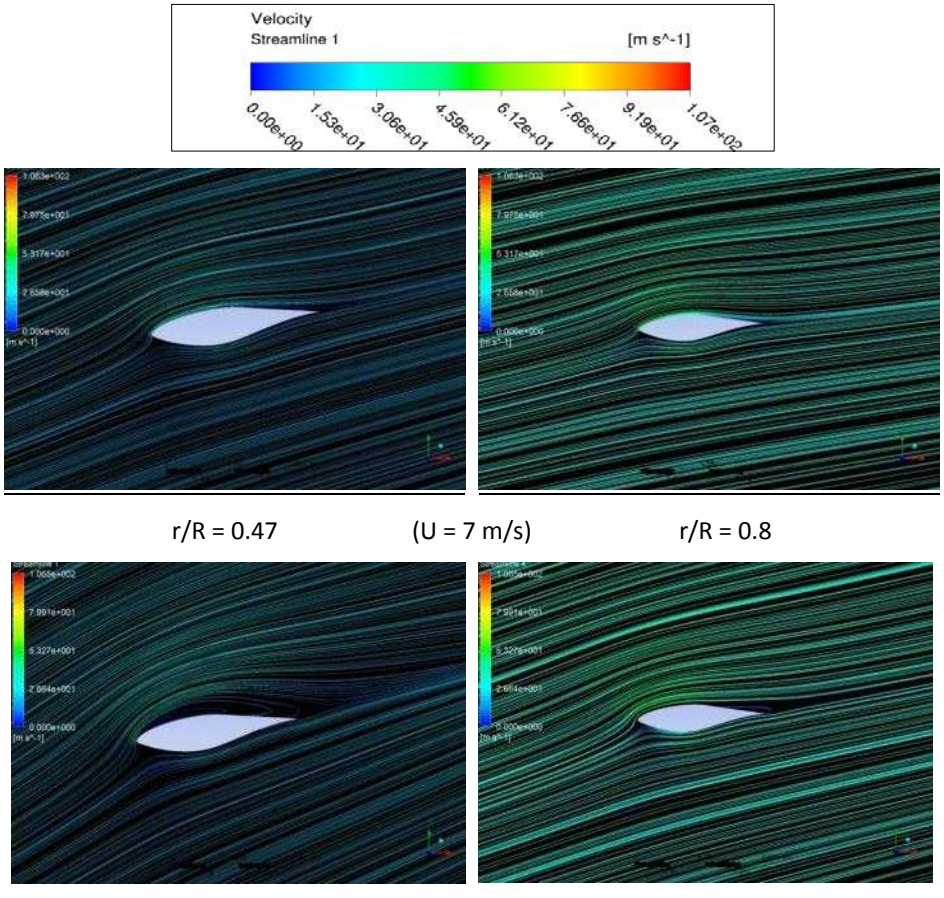

r/R = 0.47 (U = 7 m/s) r/R = 0.8

r/R = 0.47 (U = 10 m/s) r/R = 0.8

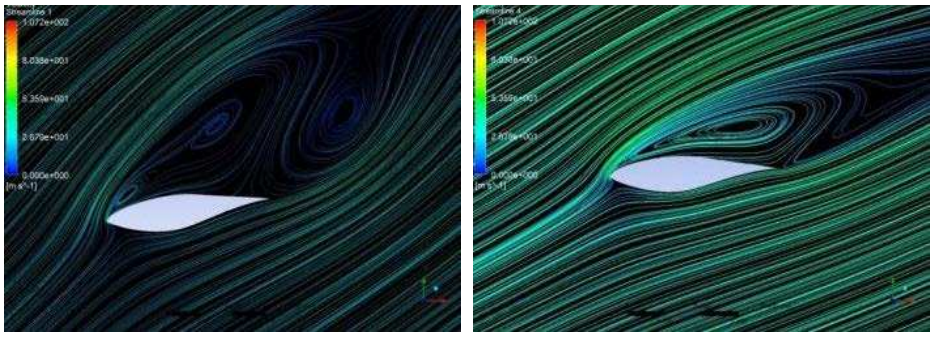

r/R = 0.47 (U = 15 m/s) r/R = 0.8 (t = 3.12s)

Figure 6. Velocity streamlines at r/R = 0.47 and 0.8 span locations. Top: wind speed = 7 m/s; middle: wind speed = 10 m/s; bottom: wind speed = 15 m/s (mean).

Figure 7 shows the surface streamlines of the wind turbine from the wind speed 7m/s to 15m/s. It can be seen that even in the wind speed = 7m/s situation there is some radial flow around the suction side of the blade. When the wind speed is higher than 13m/s, almost the whole blade is stalled. It is noted that when separation happens on the suction side of the blade, the flow becomes dominantly spanwise other than streamwise. This is because after separation, the boundary layer loses its chordwise momentum and the centrifugal force draws the flow from root to tip on the suction side of the blade. According to the figure, for this stall regulated wind turbine, even at its designed wind speed 10m/s the spanwise flow dominates more than half of the suction side of the blade. This phenomenon also shows that it is significant to simulate the full 3D blade in a rotating frame other than just study the blade sections because of the spanwise flow interactions.

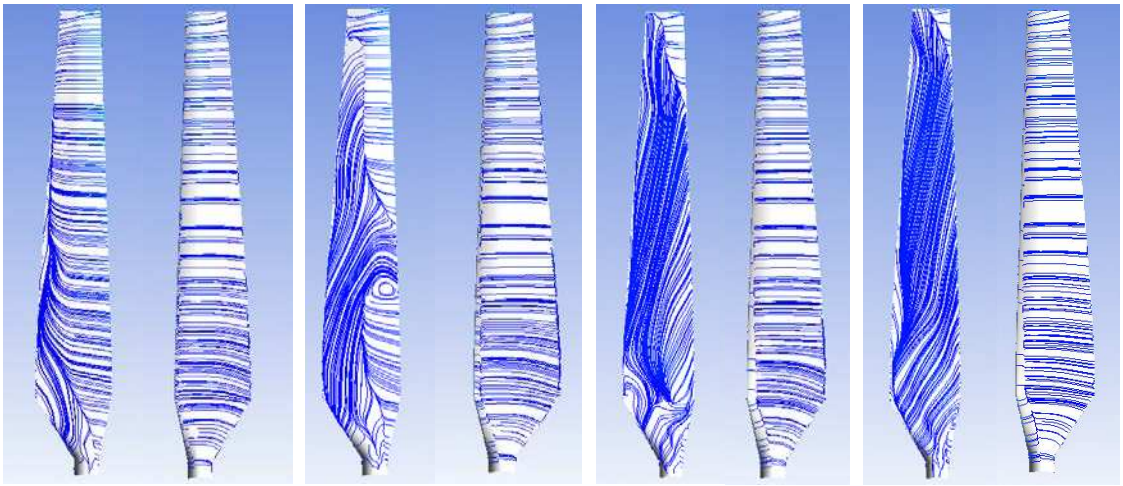

U = 7m/s U = 10m/s U = 13m/s (t = 2.04s) U = 15m/s (t = 3.12s)

Figure 7. Surface streamlines of the wind turbine from U=7m/s to 15m/s. Suction side on the left and pressure side on the right.

In conclusion, the validation case for the NREL Phase VI wind turbine shows that with proper turbulence modelling and computational mesh, the performance of the stall regulated wind turbine can be reasonably predicted, which can effectively support the flow control study later.

2D NUMERICAL STUDY of FLOW CONTROL DEVICES on S809

Methodology

Before studying the performance of the flow control devices on a rotating turbine blade, 2D simulations of the flow control devices on a blade cross-sectional aerofoil were conducted. Here the selected aerofoil is S809 located at the 80% span of the NREL PHASE VI wind turbine. The details are shown in Table 5. The microtab and the microjet are deployed at the 90% chord length position of the aerofoil section, while a 3%c divergent trailing-edge (DTE) is investigated for comparison. The detail geometries and the 2D meshes are shown in Figure 8. As noted, structured meshes were used to give high accuracy/resolution near the boundary layers and the flow control devices for the computational accuracy.

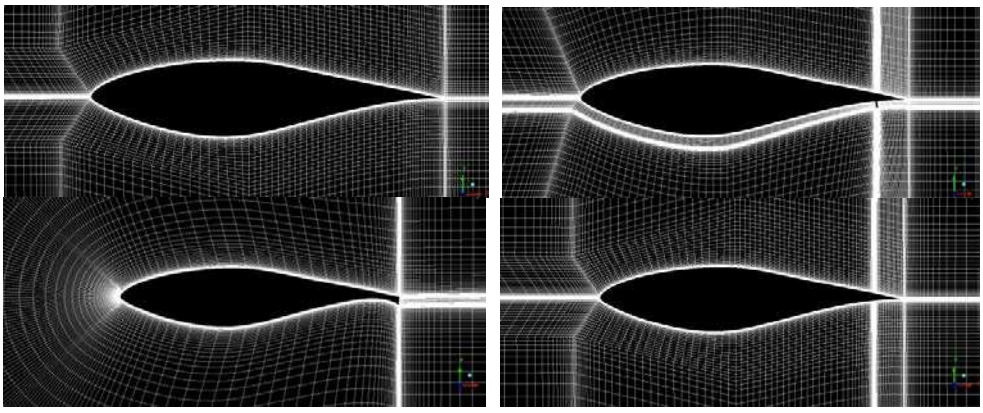

Figure 8. 2D mesh of S809 aerofoil and the aerofoil with 2% chord length microtab (top right), 3% chord length DTE (bottom left) and microjet (bottom right)

Table 5. 2D study of flow control devices on S809 aerofoil

Chosen wind turbine	NREL PHASE VI
Span location	r/R = 0.8
Rotational speed	7.54 rad/s
Sectional twist angle	2.619 degrees
Wind speed	5m/s –14m/s
Aerofoil chord length	0.457m

Reynolds number	Around 10^6
Microtab size	2% chord length
Microjet speed	60m/s
Divergent trailing-edge thickness	3% chord length

Figure 9 helps to show how flow around a 3D blade is extracted into a problem of 2D flow around a blade aerofoil section. In the figure, β is the blade tip pitch angle and $\emptyset$ is the local twist angle of the sectional aerofoil. Therefore the total pitch angle of the aerofoil chord line to the rotation plane is $\beta + \emptyset$. L and D represent the lift and drag of the aerofoil, respectively. F_r represents the resultant force from L and D. F_T represents the induced thrust force from F_r. U_r is the resultant velocity and α is the angle of attack. From the wind turbine vortex system theory (Hansen, 2000), the incoming wind flow is affected by the rotating wind turbine. So the induction factor a and a' are introduced and the resultant flow velocity can be decomposed into axial and tangential component as $U_\infty(1-a)$ and $\omega r(1+a')$ respectively. This theory is used for studying the 2D aerodynamics of the cross-sectional aerofoil of the wind turbine in the BEM method. In the present work all cases are run using CFD and proper outer boundary conditions can be used without the induction factors. The velocity inlet boundary condition is set on the far field for all 2D cases in the present work. So the relative velocity is the combination of the rotational speed at the aerofoil section ωr and the wind speed U_∞.

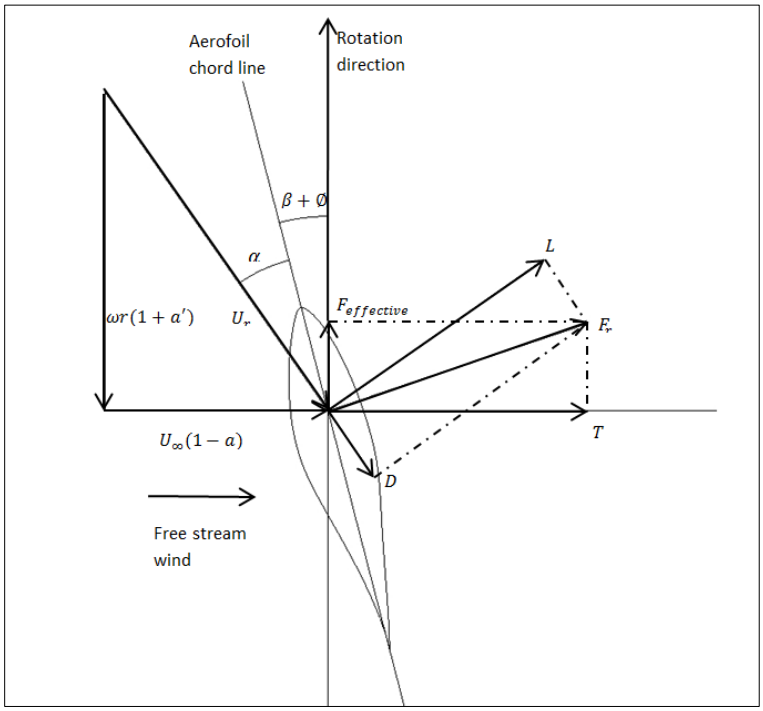

Figure 9. HAWT's cross-sectional aerofoil aerodynamic angles and forces.

Results

As mentioned above, the cross-section S809 aerofoil at the r/R = 0.8 span position of the NREL PHASE VI wind turbine is selected for the 2D flow control devices and DTE study. Considering implementation requirements for the microtab and microjet as active flow control devices, the 3mm width microtab and microjet are deployed at 90% x/C positions on the pressure side of the aerofoil.

Since the 2D aerofoil is for a wind turbine blade rather than an aircraft wing, focusing just on the lift drag ratio as in many previous literatures can be misleading. Therefore in the present study we investigate directly the effective force in the rotational direction of the blade, which drives the turbine blade around. This effective force is the final resultant force of the cross-section aerofoil contributing to the torque of the wind turbine. Figure 10 shows the effective force comparison between the S809 aerofoil with microtab, microjet and the redesigned 3% chord length DTE aerofoil. The results show that all three flow control devices give positive performance to the effective force from the aerofoil from 7m/s to 10m/s wind speed range. However at 13m/s and 15m/s conditions both DTE and microtab cases show reduction in the force while the microjet case still shows some improvement.

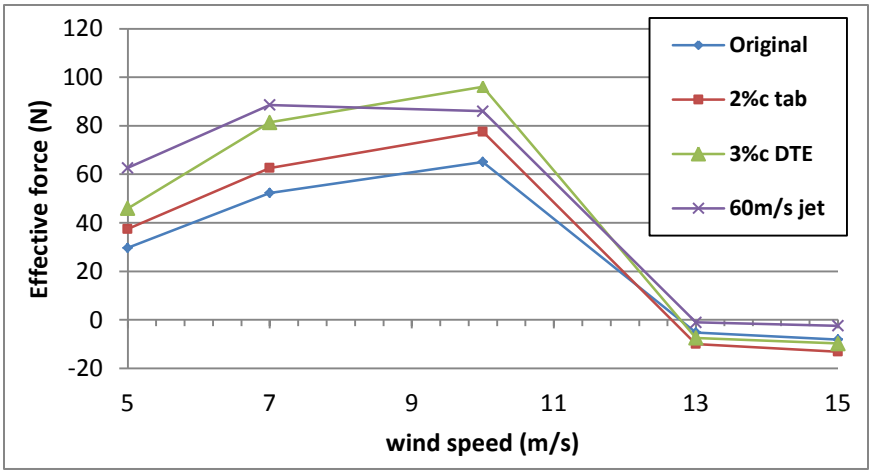

Figure 10. Effective force comparison among different trailing-edge flow control devices

The pressure coefficient comparison between different flow control devices at 7m/s, 10m/s and 15m/s wind speeds can be seen from Figure 11. The results show that the flow control devices increase the differences of the pressure coefficient between pressure side and suction side of the aerofoil near the leading edge at 7m/s and 10m/s cases. However when at 15m/s wind speed where the aerofoil is fully stalled, this condition disappears and the pressure coefficients around the leading edge of the aerofoil are very similar for all cases.

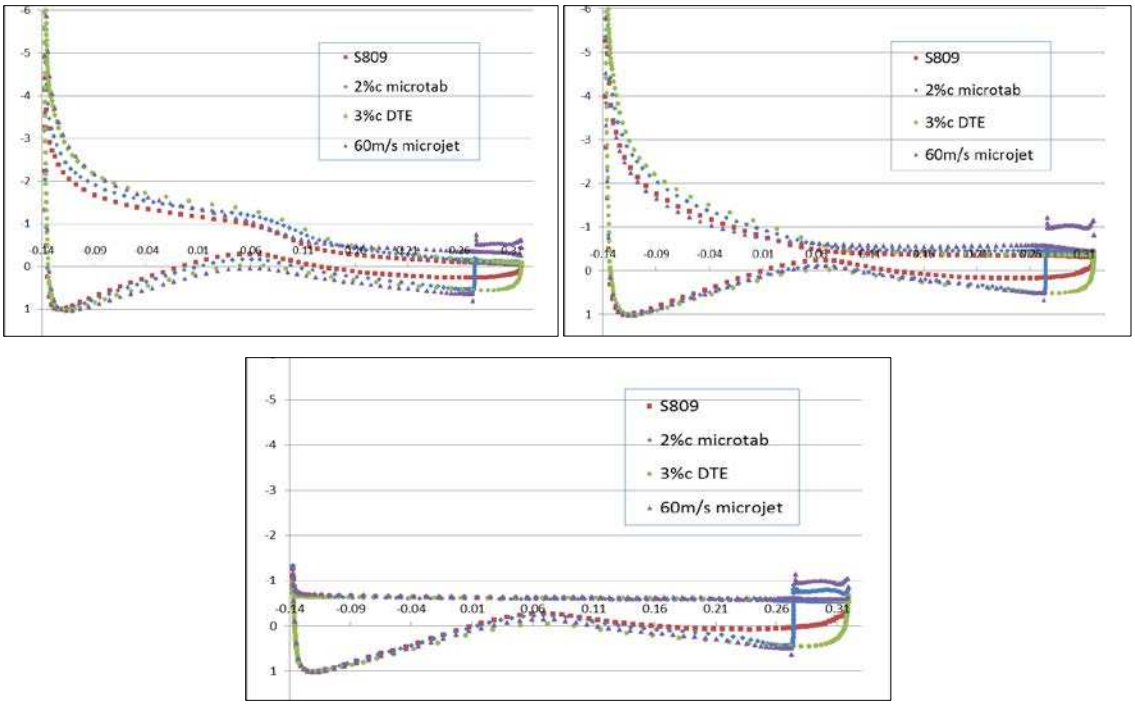

Figure 11. Pressure coefficient comparison between different flow control devices. (top left: U = 7m/s; top right: U = 10m/s; bottom: U = 15m/s)

Figure 12 to 14 show the streamlines and the gauge pressure around the aerofoil at 7m/s, 10m/s and 15m/s wind speeds respectively. Overall, the 2D computational results show that all flow control devices have positive results at non-stall wind speeds (5m/s-10m/s) for the S809 aerofoil. However in a real 3D rotating situation as shown in the last section, the flow is much more complicated with strong spanwise flows. For the higher wind speed cases, the 2D flow control results are less relevant.

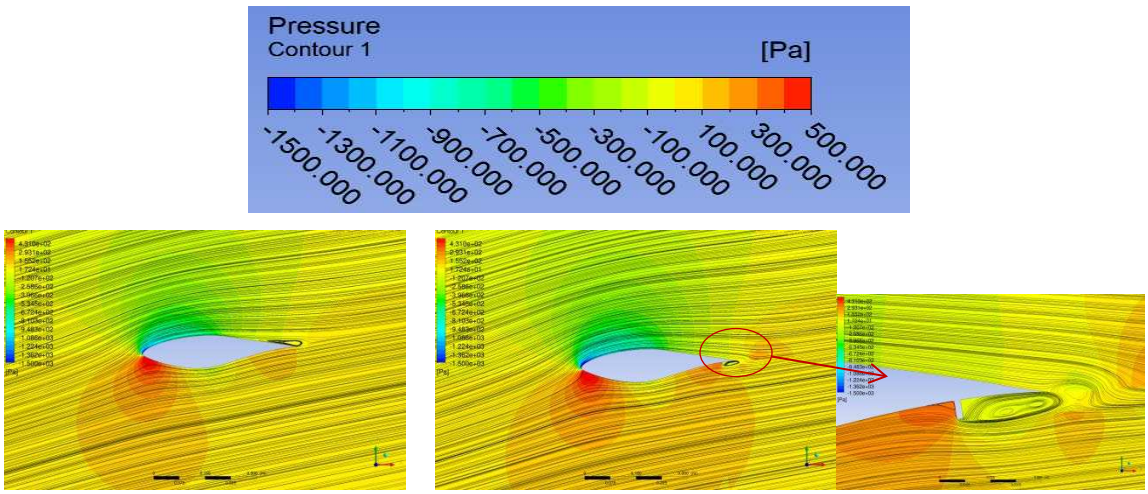

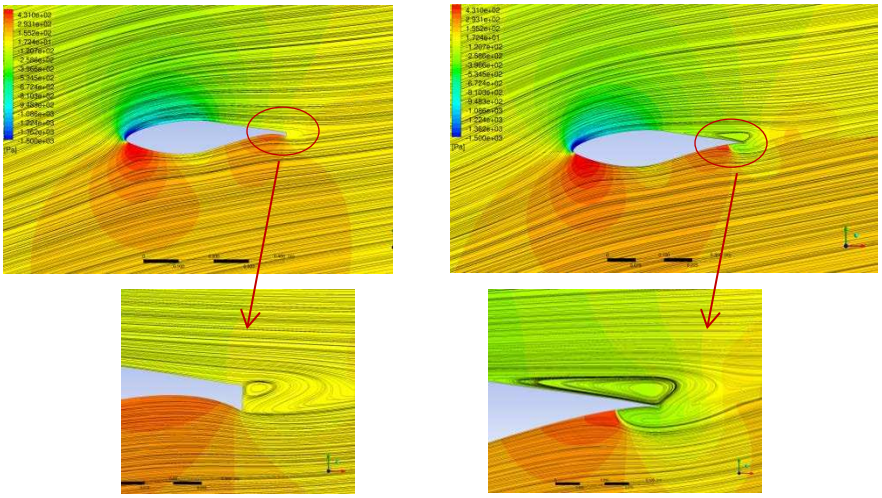

Figure 12. Streamlines overview at 7m/s wind speed. Top left: S809 aerofoil; top right: S809 with 2% chord length microtab; bottom left: S809 with 3%c DTE; bottom right: S809 with 60m/s microjet.

In Figure 12 it can be seen that there is a very small separation on the suction side of the original S809 aerofoil near the trailing-edge which is now happened at the same span section in the 3D validation case. This condition is a sign that the 2D simulation on the sectional aerofoil might not be able to fully transfer to the real situation in the 3D rotating frame situation. Moreover, it is interesting to see that the deployments of the microtab and DTE design on the S809 aerofoil effectively eliminate this small separation at 7m/s wind speed, while the 60m/s microjet makes it even larger. In Figure 13, because of the high incidence of the aerofoil at 10m/s wind speed, the flow controls are not able to cause big changes for the separations on the suction side. However at this incidence because of the changing camber of the aerofoil, these three flow control concepts still show some improvement on the effective force. When the wind speed is as high as 15m/s, the flow on the whole suction side of the aerofoil is separated (Figure 14) which leading to fast drop of the C_L and the effective force. Therefore in this situation all the trailing-edge flow control concepts are not able to improve the aerodynamic performance of the aerofoil. However because of the large separation which starting from the leading edge on the suction side, the leading edge microjets can be concerned as the separation control devices for improving the aerofoil performance, which would be studied later.

In conclusion, from the 2D flow control devices study on S809 aerofoil it can be seen that in the non-stall situation all flow control devices can effectively improve the performance of the aerofoil which contributing to the final torque of the blade. It is also worth mentioning that in lower wind speeds such as 5m/s and 7m/s, some of the flow control devices can increase as high as 50%-100% of the performance. However from the validation study it is known that the spanwise flow is also strong for this wind turbine, which is totally ignored in the 2D study. Therefore it is necessary to carry out 3D study on the flow control devices in an actual rotating situation, in order to find whether the performance gain in the 2D flow control study is true.

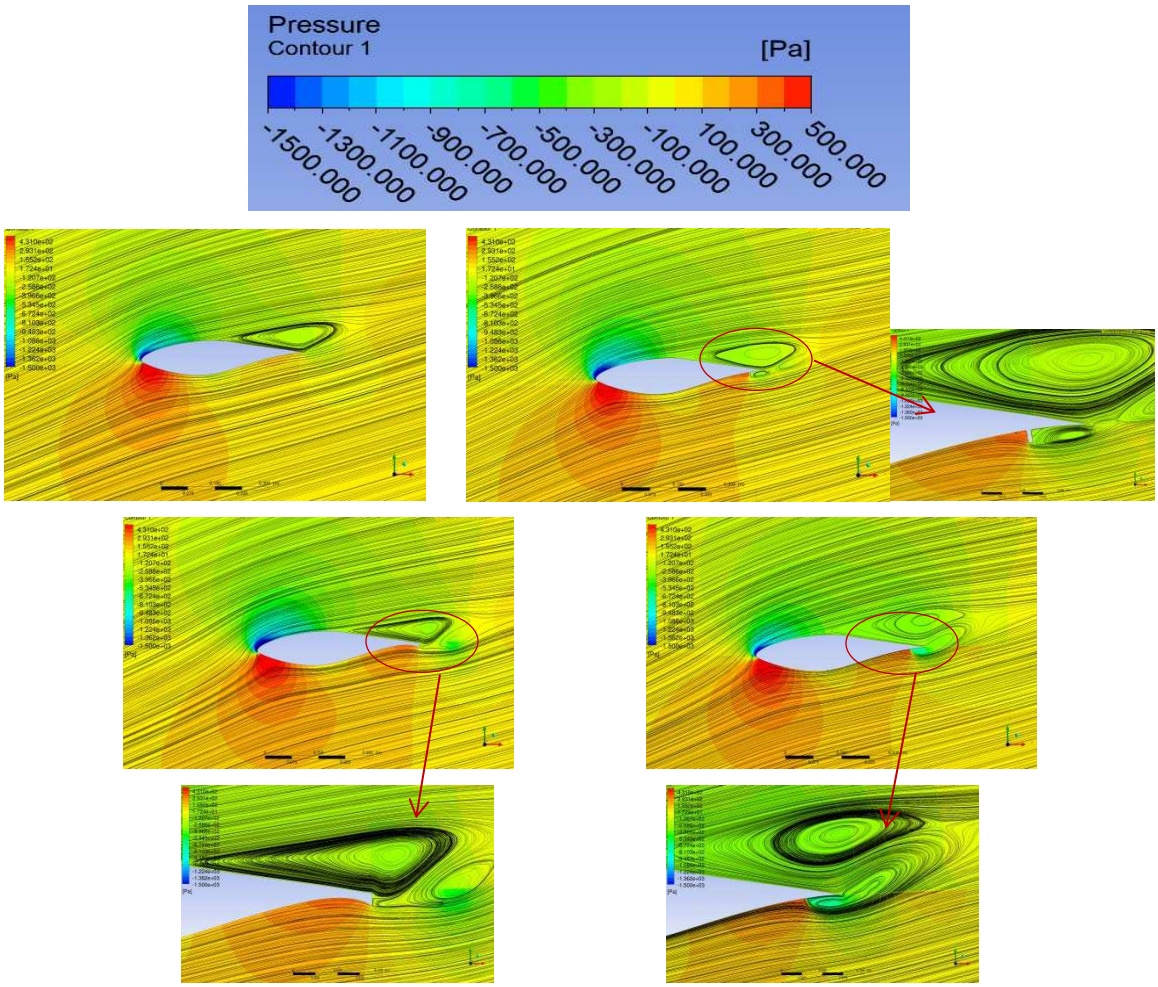

Figure 13. Streamlines overview at 10m/s wind speed. Top left: S809 aerofoil; top right: S809 with 2% chord length microtab; bottom left: S809 with 3%c DTE; bottom right: S809 with 60m/s microjet.

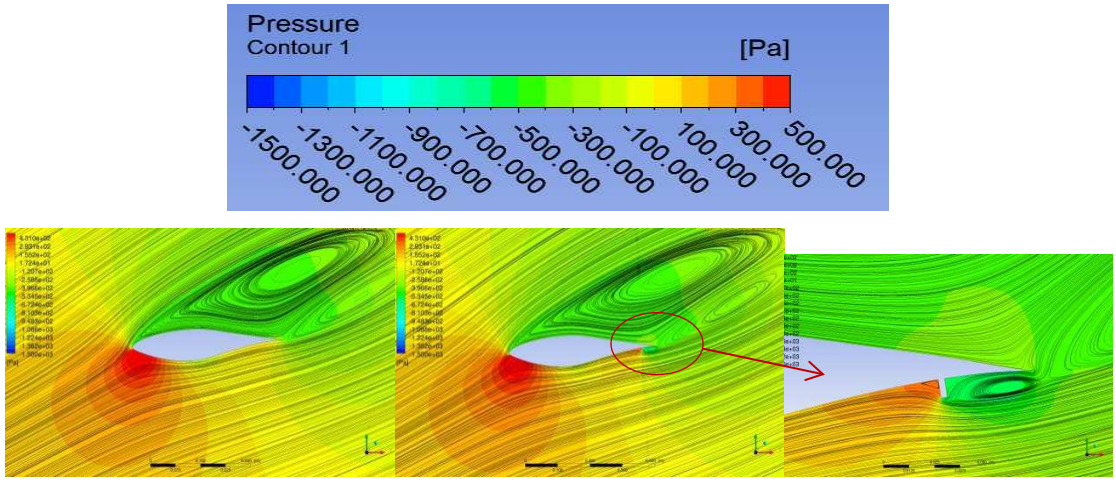

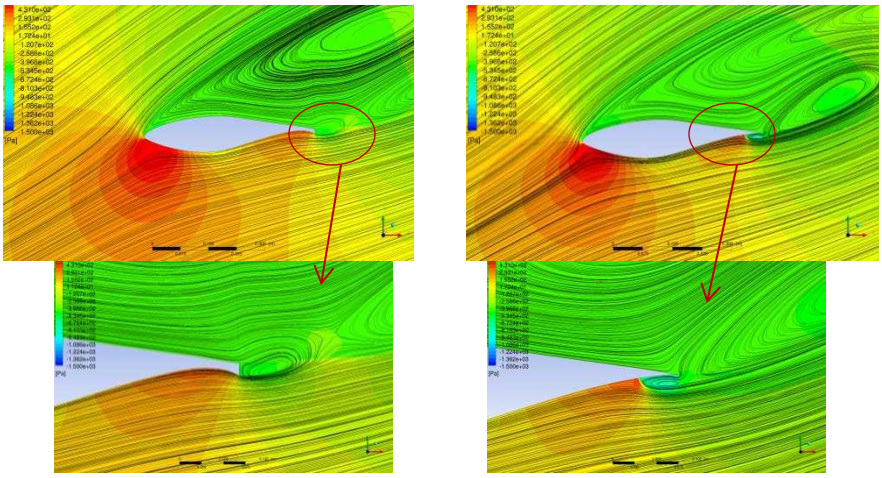

Figure 14. Streamlines overview at 15m/s wind speed. Top left: S809 aerofoil; top right: S809 with 2% chord length microtab; bottom left: S809 with 3%c DTE; bottom right: S809 with 60m/s microjet.

3D NUMERICAL STUDY of MICROJETS, MICROTABS and DTE

Methodology

The methodology for the 3D simulation of the NREL Phase VI wind turbine with different flow control devices and the 3%c DTE is the same as presented for the validation case. The boundary conditions and turbulence model are the same. In order to meet the wall y^+ requirement the mesh size of the blade with microtab is increased to 8.2 million and a 6.3 million grid for the blade with microjet and a 4.5 million grid for the blade with 3% chord length DTE. Figure 15 shows the mesh overview for the blade with different flow control devices.

The microtab and the microjet are installed/activated along the blade from 70%-97% along the blade span. The reason for this choice of span location is due to the fact that this is the most energy/torque generating part of the blade, which is also the most highly loaded part. For the same reason the DTE is implemented between 70%-100% span.

As mention above, the flow of NREL Phase VI wind turbine blade becomes fully unsteady when wind speed exceeds 13m/s. Therefore here the unsteady simulations are also carried out for 13m/s and 15m/s wind speed cases with a 0.0006s physical time-step size . Other wind speed cases are simulated as steady flows.

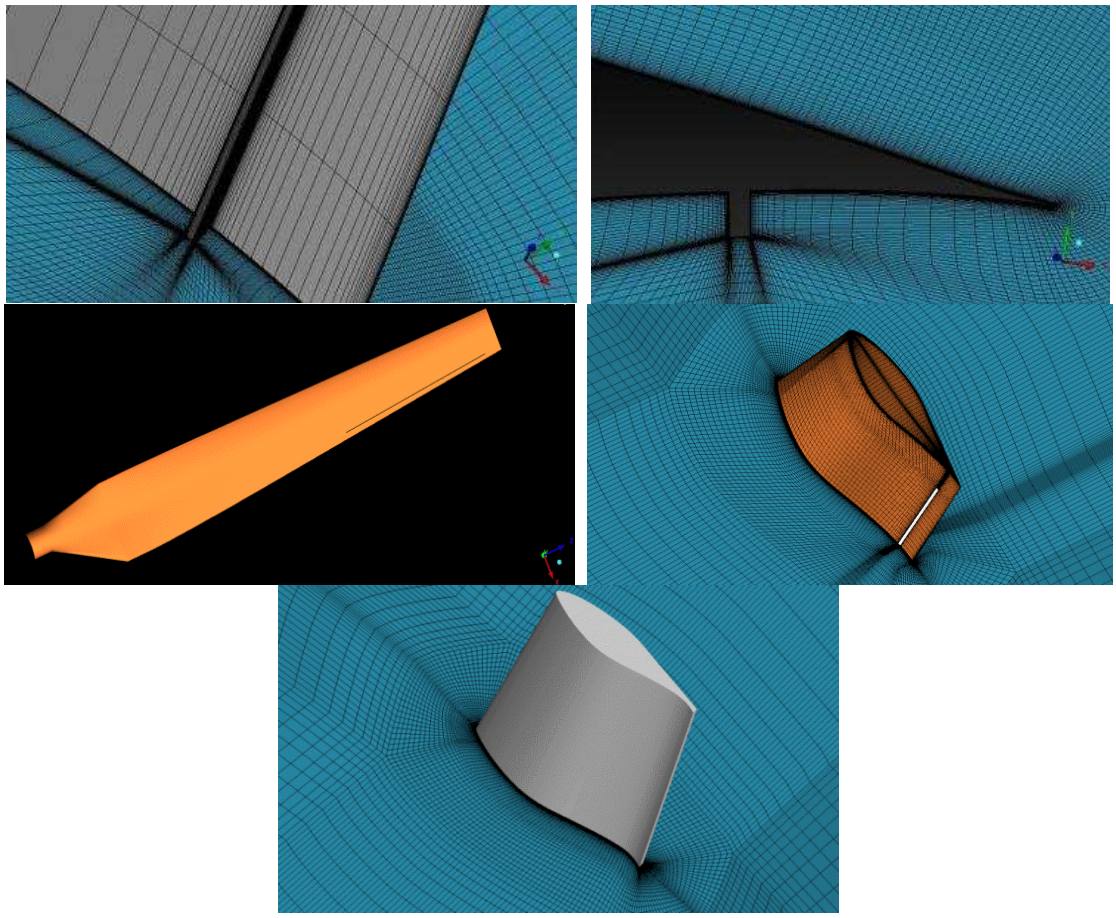

Figure 15. Top : mesh overview of the blade with 2%c microtab from 70%-97% span; middle: mesh overview of the blade with microjet from 70%-97% span; bottom: mesh overview of the blade with 3% DTE from 70% to tip.

Results

The results of the torque and power coefficient are shown in Figure 17 and 18. The 3D results show some marked difference from the 2D results. For the 5m/s case, the improvement due to flow control from the 3D results is much less than that from the 2D case. Moreover, the 3% DTE shows best performance in the 2D aerofoil study while in the 3D rotating blade study it shows the worst performance. As mentioned before, all the cases for 13m/s and 15m/s wind speeds are run in unsteady flow simulations. A sample of the momentum coefficient convergence history and the torque calculation can be found in Figure 16.

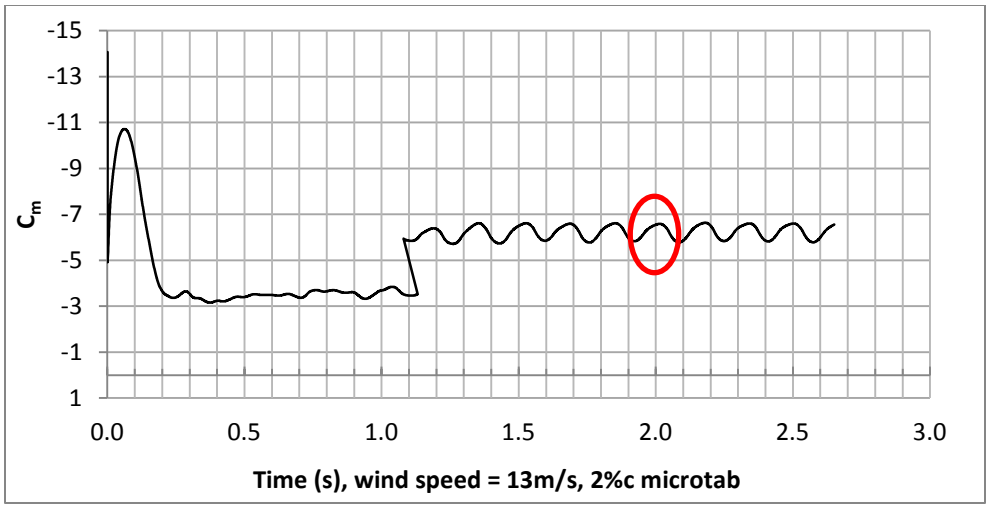

Figure 16. C_m convergence history for the wind turbine with 2%c microtab at 13m/s wind speed, the final mean torque is calculated at one cycle as shown in the graph.

In summary, referring to the power coefficient comparison it can be seen that in the 3D rotating situation, the trailling-edge flow control devices improve a maximum of 29% in C_p than the original blade(60m/s microjet at 5m/s). Moreover, even at 10m/s, which is the design speed of the blade, the 2%c height microtab and the 60m/s microjet increase C_p by 22.2%. However, similar as the 2D results, in the stall wind speed range (higher than 10m/s) the flow control devices become ineffective.

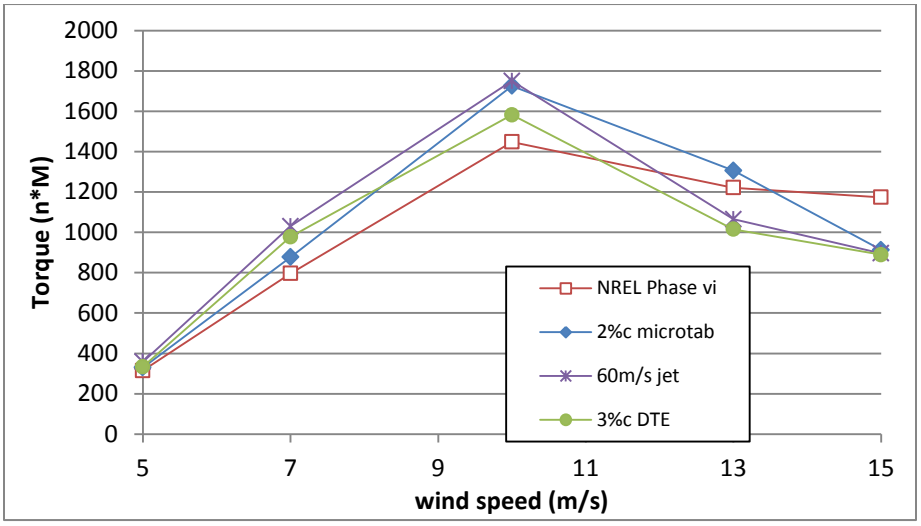

Figure 17. Torque comparison between the original blade and the blade with different flow control devices.

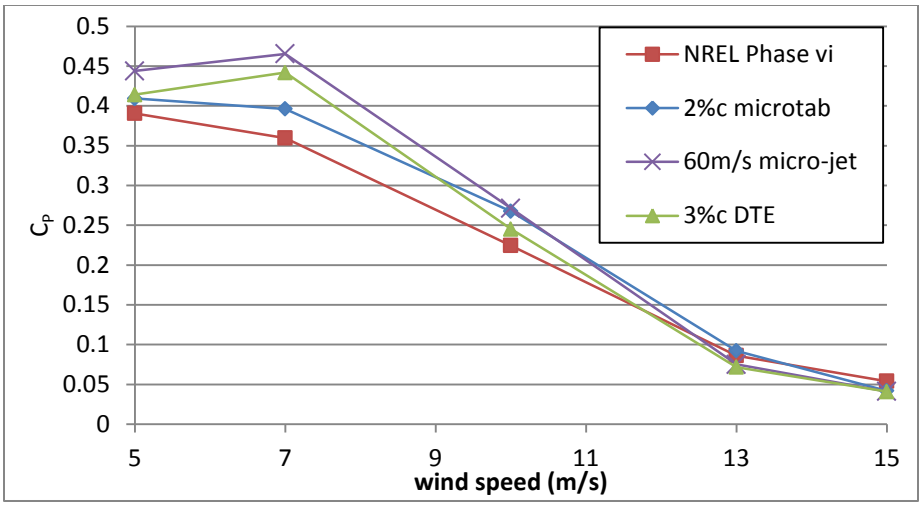

Figure 18. Power coefficient comparison.

Cross-sectional pressure coefficient (C_p) comparison

Figures 19, 20 and 21 show the cross-sectional aerofoil pressure coefficient C_p at two different span positions, r/R =0.47 and r/R = 0.8 respectively. From the figures it can be seen that the trailing-edge flow control devices not only change the C_p at where they are deployed but also influence the C_p at the lower part of the blade.

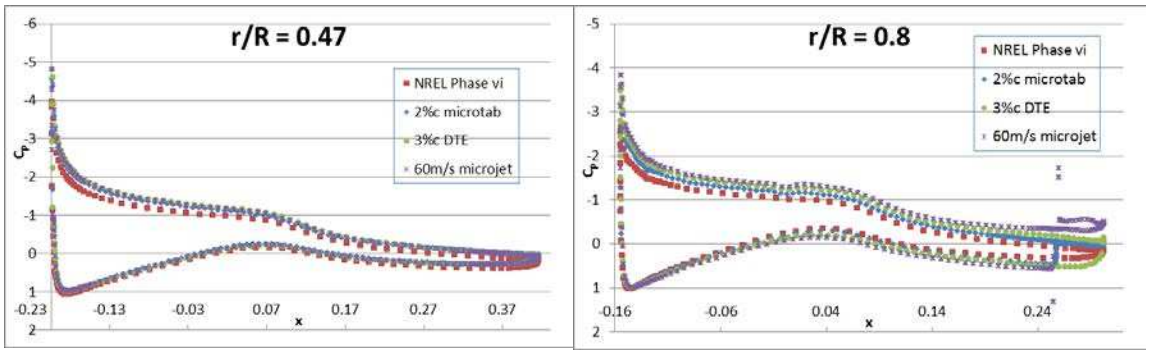

Figure 19. Sectional aerofoil pressure coefficient comparison at wind speed = 7m/s.

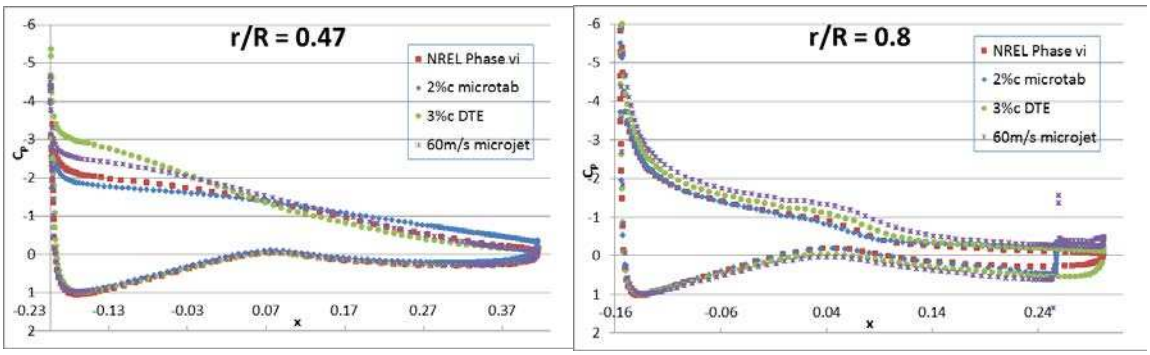

Figure 20. Sectional aerofoil pressure coefficient comparison at wind speed = 10m/s.

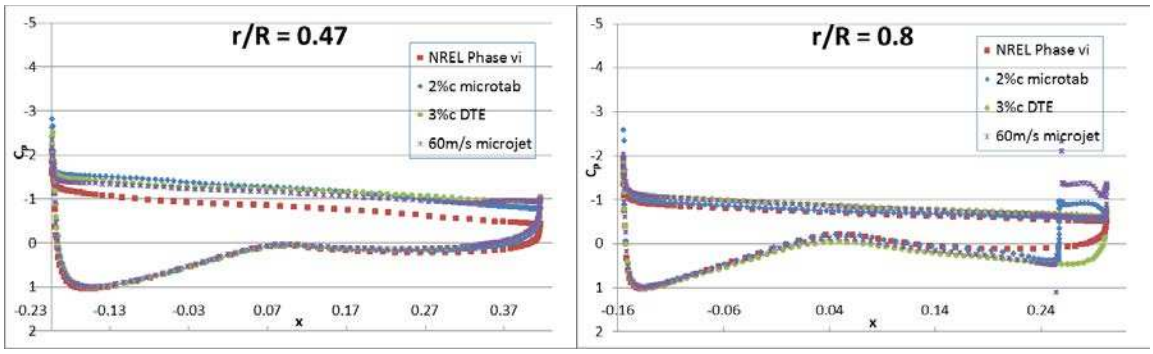

Figure 21. Sectional aerofoil pressure coefficient comparison at wind speed = 15m/s.

The left graph of Figure 19 shows that at 7m/s wind speed, the aerofoil suction side C_p at r/R = 0.47 section is silghtly changed by after deploying the flow control concepts. The changes from all three kinds of concepts are quite similar which leading to small improment of the lift force of the sectional aerofoil. The right graph of Figure 19 shows that at r/R = 0.8 section, where the flow control devices are deployed, all flow control concepts improve the aerodynamic lift force of the sectional aerofoil while the 60m/s outlet speed microjet shows the largest improvement.

At 10m/s wind speed, as can be seen from the left graph of Figure 20, the r/R = 0.47 aerofoil section of the blade begins to stall. The 3% chord DTE and microjet delay the stall slightly while the microtab enhances the sectional stall action. At r/R = 0.8 section, the C_p of the sectional aerofoil with the microtab is quite similar as the original blade while DTE and microjet show show improvement of the aerodynamic lift force.

Figure 21 shows that at 15m/s wind speed, most area of the blade is in stall action even for the r/R = 0.8 section. The left graph of Figure 21 shows that at r/R = 0.47, where no flow control are deployed, all three kinds of flow controls improve the sectional aerodynamic lift force slightly. At r/R = 0.8 section, which is shown in the right graph, the C_P of the original blade and with flow controls is quite similar where just some minor improvements due to the flow controls.

The C_p investigation shows that the flow controls also lead to aerodynamic changes at lower span of the blade where no flow control is deployed which can be seen from the analysis of r/R = 0.47 section shown above. The driving force of the wind turbine is the lift force from the sectional aerofoils and the lift force is produced from the pressure differences between the pressure side and suction side of the aerofoil. Therefore from Figures 19 to 21, the enlarged pressure differences to some extent explain why the flow control devices can improve the power output of the wind turbine.

Surface wall shear streamlines overview (Suction side on the left, pressure side on the right)

Figures 22-24 show the skin friction lines on the blade surface. It is quite interesting to note that at the 10m/s wind speed, which is the design speed of the blade, the flow control devices delay stall of the blade on the suction side. The flow on the suction side seperates from 0 to around 0.9 span of the original blade. However for the blade with the 60m/s microjet, the seperation on the suction side happens from 0 to 0.75 span. When the wind speed is 15m/s, because of the higher incidence, seperation appears on the suction side along the whole blade and the flow control devices therefore lose their effectiveness (see Figure 24). From these figures, it can be

seen that at 10m/s and 15m/s wind speed, when separation happens on the suction side of the blade, the flow becomes spanwise other than streamwise. When separation happens, the centrifugal force draws the flow from root to tip on the suction side of the blade. According to the figures, for this stall regulated wind turbine, even at its designed wind speed 10m/s the spanwise flow occupies more than half area of the suction side of the blade. This illustrates that the 2D assumption in a stationary frame can misrepresent the flow with misleading results and conclusions.

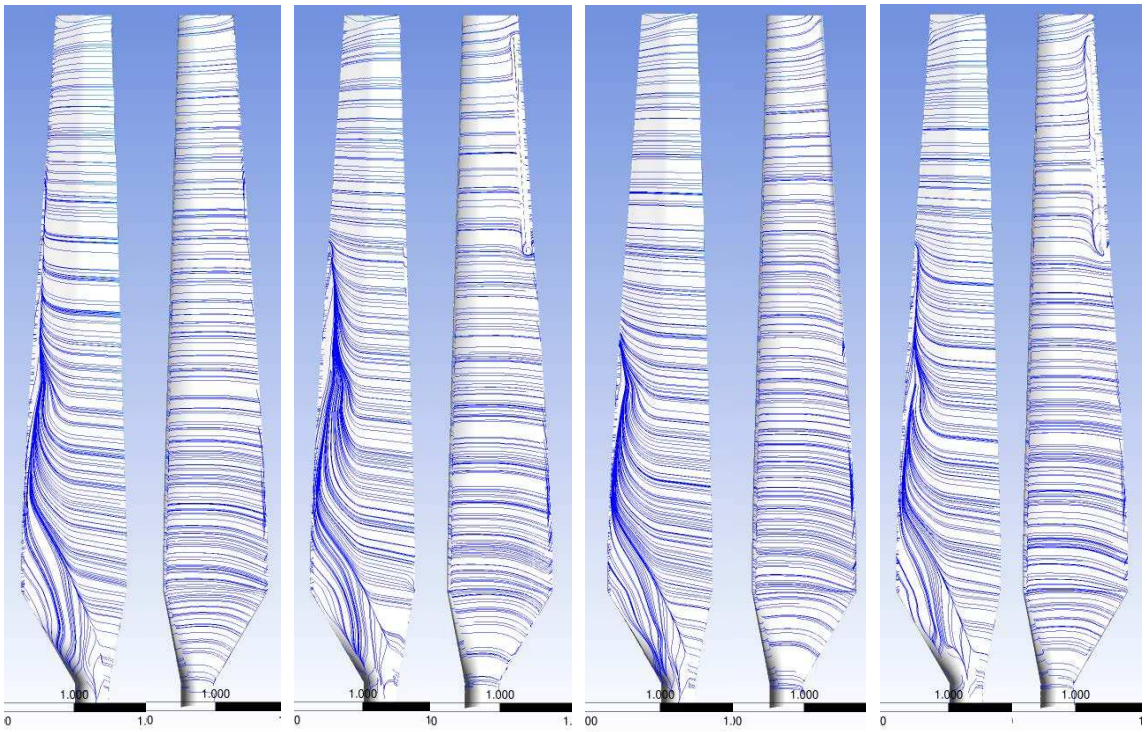

Original 2%c microtab 3%c DTE 60m/s microjet

Figure 22. Surface wall shear streamlines comparison at wind speed = 7m/s.

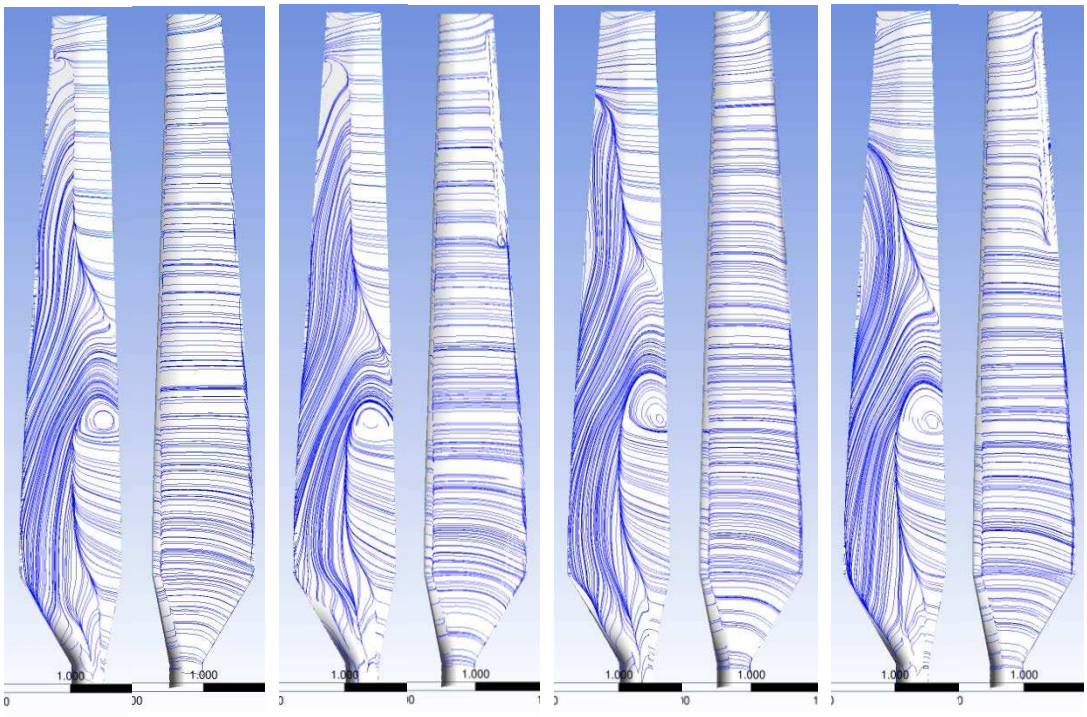

Original 2%c microtab 3%c DTE 60m/s microjet

Figure 23. Surface wall shear streamlines comparison at wind speed = 10m/s.

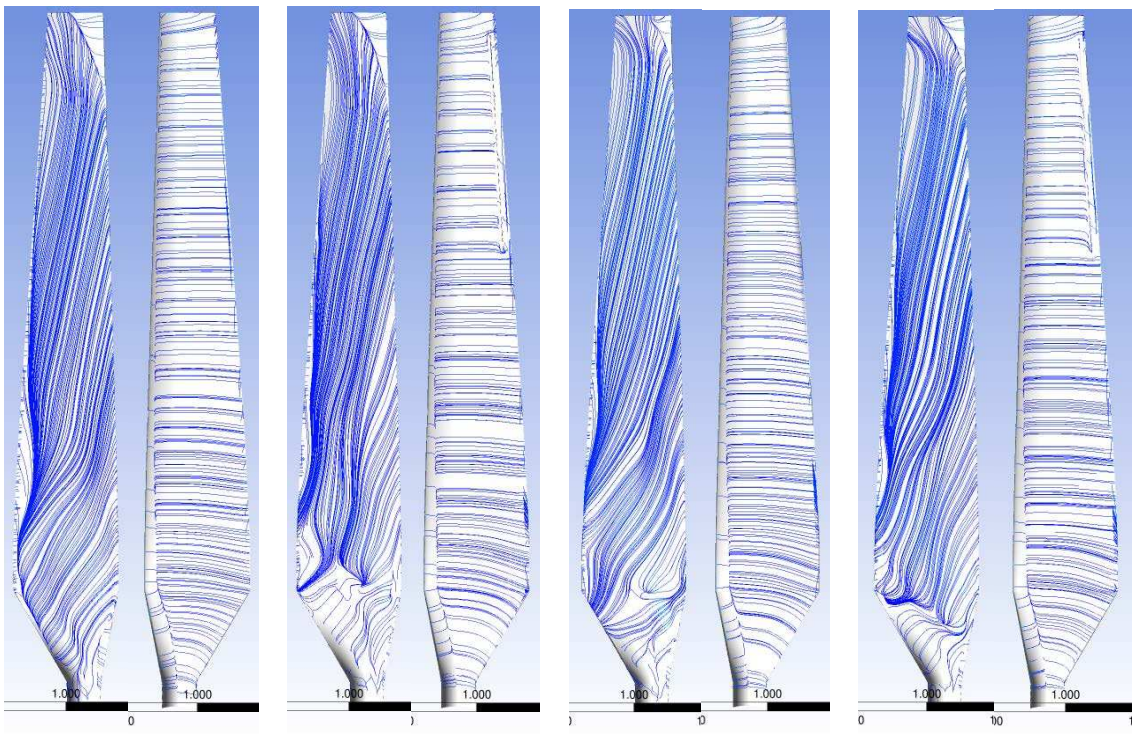

Original 2%c microtab 3%c DTE 60m/s microjet

Figure 24. Surface wall shear streamlines comparison at wind speed = 15m/s.

In summary, from the surface friction streamlines it can be seen that at lower wind speed range where the blade is not fully stalled and the spanwise flow is not dominanting on the suctionside, the flow control devices can effevtively improve the aerodynamic performance of the blade. However, when the wind turbine is fully stalled and all the suction side of the blade is dominated with spanwise flow, all three kinds of flow control devices are not able to further increase the power output of the blade because the aerodynamic performance of the sectional aerofoils are no longer valid at this situation.

Comparison of surface pressure coefficient between 2D and 3D results for microtab control

Figure 25 shows the comparison of the surface pressure coefficient at the same r/R = 0.8 span at 7m/s for 2%c microtab. As can be seen, the 2D surface pressure show a much larger pressure differece (higher loading) near the leading edge as compared to the 3D result. This explains the overprediction of the effectiveness of the microtab when the 2D assumption is made. This gives the reason why in 3D rotating frame simulations of the flow control devicets are not able to reproduce the performance improvement predicted in 2D sectional simulations (Figure 10 and 17).

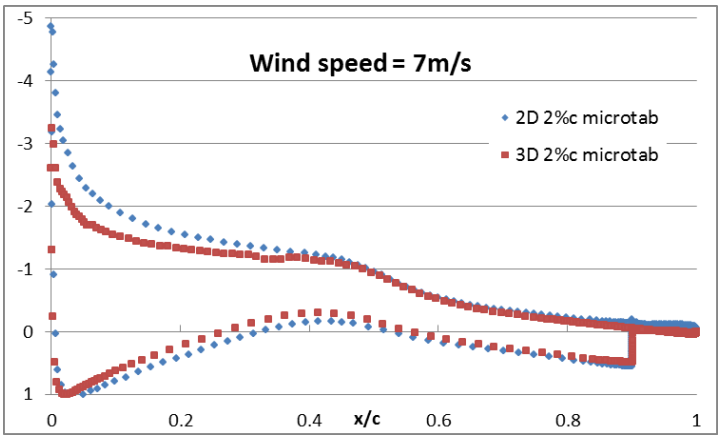

Figure 25. Pressure coefficient comparison between the 2D and 3D results on the r/R = 0.8 section.

Cross-sectional flow streamlines comparison at r/R = 0.8 span position

Figure 26 shows the cross-sectional streamlines at r/R = 0.8 position which is the same position as the 2D simulations. Compared to the 2D study above, the flow condition on the suction side is different from the 2D simulations. In the 3D simulation the flow is fully attached on the suction side while the 2D simulation shows a small seperation near the trailling-edge. The streamlines near the trailling-edge on the pressure side of the 3D simulation is very similar as the 2D simulations.

Figure 27 shows the velocity streamlines of the r/R = 0.8 span section at 10m/s wind speed. The 3D results also show a much smaller seperation flow on the suction side compared to the 2D simulation results. An interesting point is that with deploying different flow control devices the flow on the suction side can be changed. The 2%c height microtab sligtly enlarge the seperation on the suction side while the 3%c DTE reduces the detached area of the flow on the suction side

and the 60m/s microjet even lead to re-attached flow near the trailing-edge on the suction side. This condition can also be observed in Figure 23.

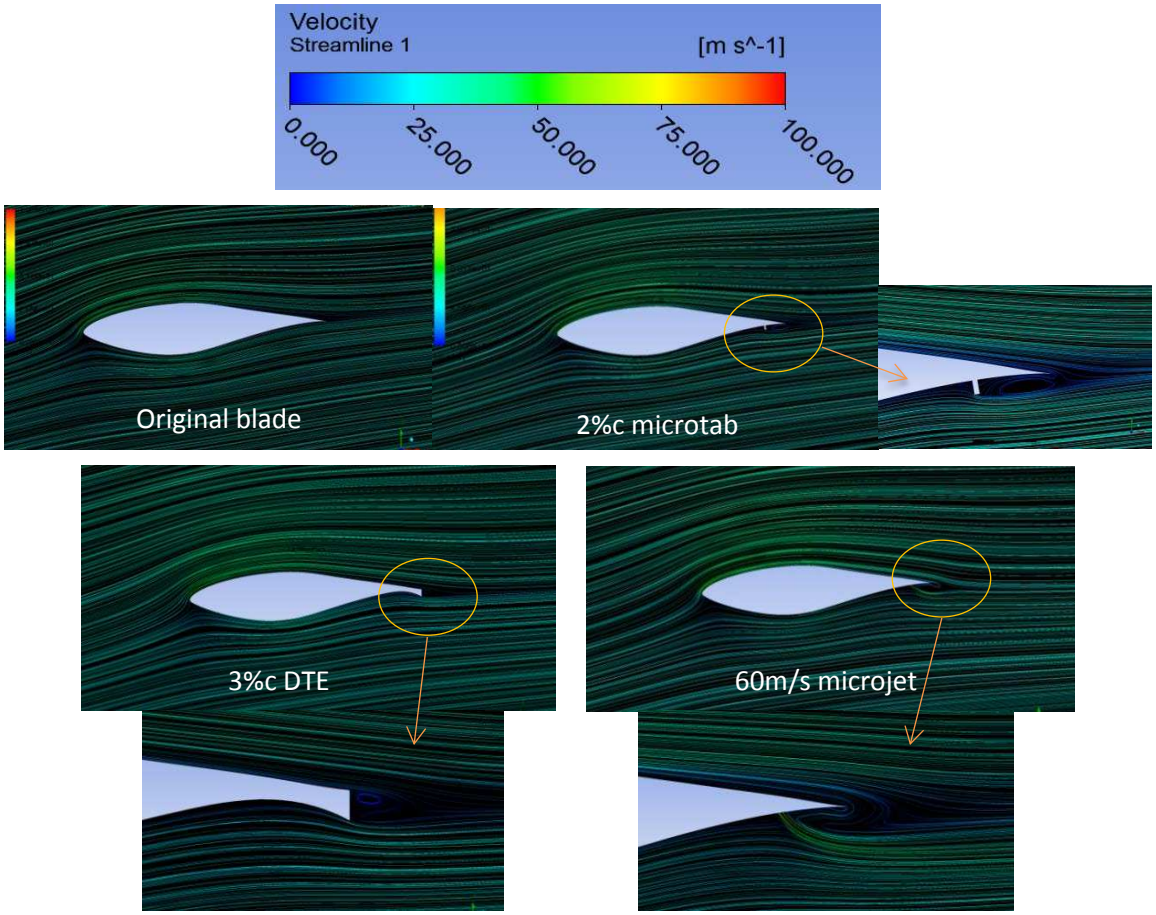

Figure 26. Cross-sectional flow streamlines comparison at 0.8 span at wind speed = 7m/s.

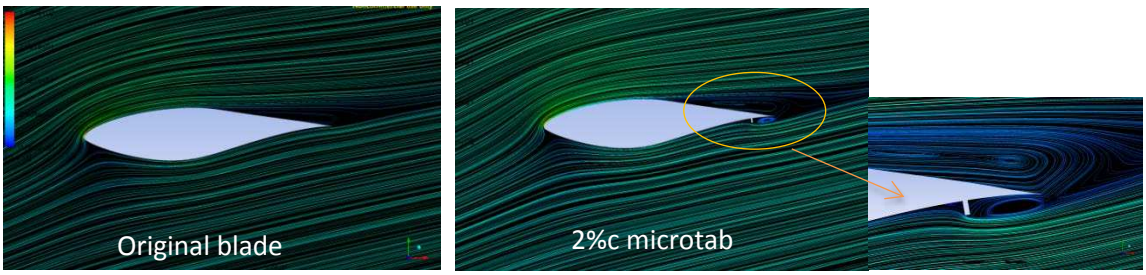

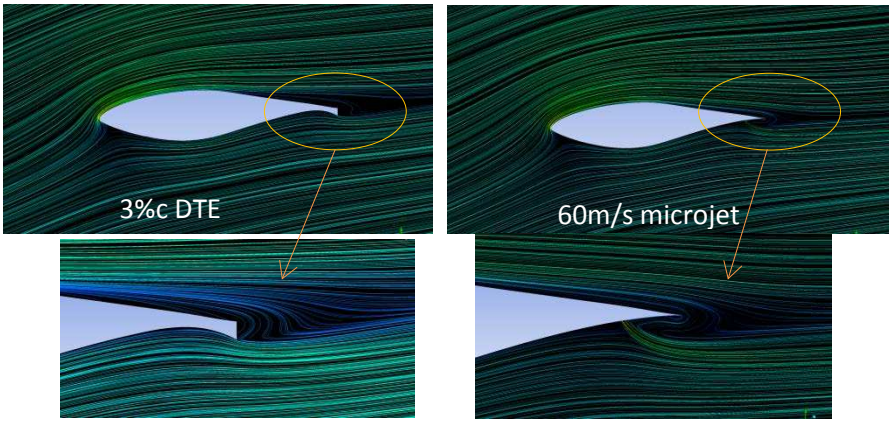

Figure 27. Cross-sectional flow streamlines comparison at 0.8 span at wind speed = 10m/s.

For the 15m/s wind speed case, because the spanwise flow dominates the whole suction side of the blade therefore 2D cut-plane view of the streamlines around the r/R = 0.8 span section is not able to truly show the flow conditions. Therefore here the cross-sectional flow streamlines at 15m/s wind speed is not included.

3D surface pressure contour comparison

Figure 28 shows the surface pressure of the original blade and the blade with different flow control devices at the rated wind speed 10m/s. The suction side is on the left while the pressure side is on the right in the figure. It can be seen that at the rated wind speed, the DTE shows the biggest effects on increasing the pressure near the trailing edge on the pressure side at 10m/s. From the pressure contour plots it can be seen that DTE and microjet alter more significantly the pressure distribution on the suction side of the blade when compared to the original one. The effect of the microtab is relatively more localized.

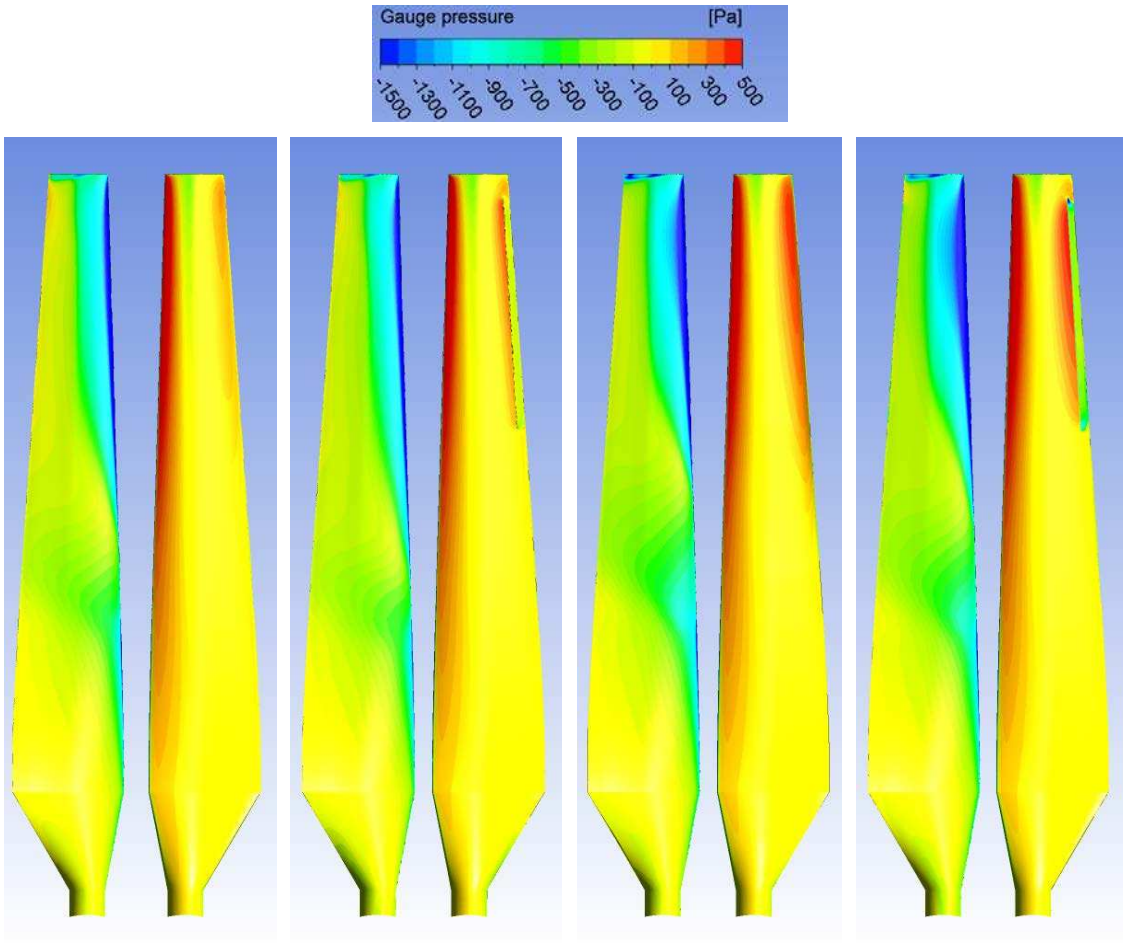

Figure 28. Surface pressure comparison at wind speed = 10m/s.

Conclusions

A stall-regulated NREL Phase VI wind turbine has been investigated with three trailing-edge flow control devices, namely, microtab, microjet and divergent trailing-edge. A validation study was first carried out and the results showed reasonable comparison with the experimental results for a range of wind speed conditions. It was found that for the higher wind speed cases at 13 m/s and 15 m/s, the flow around the blade is unsteady and becomes periodic. The averages of the torque were found in better agreement with the experimentally measured torques than that from the steady state solution. While the pressure side is dominated by chordwise flows, strong spanwise flows were found from the skin friction lines on the suction sides of the blade. This spanwise flow is getting progressively stronger as the wind speed is increased.

Before simulating the flow control devices in full 3D in the rotating framework, the 2D study of flow control devices on the S809 aerofoil at r/R = 0.8 position of the wind turbine was carried out. The results show that in lower wind speed range when the blade is dominated by attached flows, the flow control devices can effectively improve the performance/torque by as much as 80%.

For more accurate prediction of the effects of the flow control devices, 3D study of flow control devices on this blade in a rotating framework is carried out. The benefit from the flow control devices is much less than the 2D cases. For example, at the 5m/s wind speed situation, the 2D simulations show large improvement by deploying the flow control devices but the 3D simulations show very slight improvement compared to the original blade. We conclude that, for flow control study, it is essential to include the 3D flow effects and 2D simulations are not reliable for performance prediction. This is attributed to the strong spanwise flow on the suction side after flow separation.

Overall, it can be seen that deploying trailing-edge flow control devices can effectively improve the power output of a stall-regulated wind turbine from the more reliable 3D simulation in the rotating framework. The 60m/s microjet is more effective at the lower wind condition while the 2%c microtab is more effective at the higher wind speed condition. However this conclusion is limited since only limited range of parameters have been studied for the microtabs and microjets. Due to the requirement of extra power and system for microjets, it seems that the microtab concept is more feasible in practice.

In the present study, the design parameters for the microtab height, the microjet velocity, and the DTE thickness were chosen from a small number of numerical tests. These parameters along with other variables may be further tested and optimized in future studies. This study is on a relatively small sized stall-regulated wind turbine. Further study of the trailing-edge flow control can be conducted for larger (higher Reynolds number) variable-speed pitch control wind turbines, which dominate the currently installed wind turbines. An interesting line of research is the Reynolds number effects on the performance of the flow control devices.

References

Baker, J. P., Mayda, E. A., & Van Dam, C. P. (2006). Experimental analysis of thick blunt trailing-edge wind turbine airfoils. *Journal of Solar Energy Engineering*, *128*(4), 422-431.

Barlas, T. K., & Van Kuik, G. A. M. (2010). Review of state of the art in smart rotor control research for wind turbines. *Progress in Aerospace Sciences*,*46*(1), 1-27.

Blaylock, M., Chow, R., Cooperman, A., & Dam, C. P. (2014). Comparison of pneumatic jets and tabs for active aerodynamic load control. *Wind Energy,17(9)*, 1365-1384.

Cooperman, A. M. (2012). *Wind tunnel testing of microtabs and microjets for active load control of wind turbine blades*.

Cooperman, A. M., Chow, R., Johnson, S. J., & van Dam, C. P. (2011). Experimental and computational analysis of a wind turbine airfoil with active microtabs. In *Proceedings of the 49th AIAA Aerospace Sciences Meeting including the New Horizons Forum and Aerospace Exposition, Orlando, FL, USA* (pp. 4-7).

Cooperman, A., Blaylock, M., & van Dam, C. P. (2014). Experimental and simulated control of lift using trailing edge devices. In *Journal of Physics: Conference Series* (Vol. 555, No. 1, p. 012019). IOP Publishing.

Esfahanian, V., Pour, A. S., Harsini, I., Haghani, A., Pasandeh, R., Shahbazi, A., & Ahmadi, G. (2013). Numerical analysis of flow field around NREL Phase II wind turbine by a hybrid CFD/BEM method. *Journal of Wind Engineering and Industrial Aerodynamics*, *120*, 29-36.

Gai, S. L., & Palfrey, R. (2003). Influence of trailing-edge flow control on airfoil performance. *Journal of aircraft*, *40*(2), 332-337.

Hansen, M. O., & Madsen, H. A. (2011). Review paper on wind turbine aerodynamics. *Journal of fluids engineering*, *133*(11), 114001.

Henne, P. A., & GREGG, III, R. D. (1991). New airfoil design concept. *Journal of Aircraft*, *28*(5), 300-311

Hurley, O. F., Chow, R., Blaylock, M. L., & Van Dam, C. C. P. (2016). Blade Element Momentum Based Study for Active and Passive Microjets Systems on the NREL 5-MW Turbine. In *34th Wind Energy Symposium* (p. 1263).

Kinzel, M. P., Maughmer, M. D., & Lesieutre, G. A. (2007). Miniature Trailing-Edge Effectors for Rotorcraft Performance Enhancement. *Journal of the American Helicopter Society*, *52*(2), 146-158.

Lee, H., & Kroo, I. M. (2006). Two dimensional unsteady aerodynamics of miniature trailing edge effectors. *AIAA paper*, *1057*, 9-12.

Li, Y. C., Wang, J. J., & Hua, J. (2007). Experimental investigations on the effects of divergent trailing-edge and Gurney flaps on a supercritical airfoil.*Aerospace Science and Technology*, *11*(2), 91-99.

Liebeck, R. H. (1978). Design of subsonic airfoils for high lift. *Journal of aircraft*, *15*(9), 547-561.

Macquart, T., Maheri, A., & Busawon, K. (2014). Microtab dynamic modelling for wind turbine blade load rejection. *Renewable Energy*, *64*, 144-152.

Mahu, R., Popescu, F., Frunzulică, F., &Dumitrache, A. (2011). 3D CFD Modeling and Simulation of NREL Phase VI Rotor. In *AIP Conference Proceedings* (Vol. 1389, p. 1520).

Mo, J. O., & Lee, Y. H. (2012). CFD Investigation on the aerodynamic characteristics of a small-sized wind turbine of NREL PHASE VI operating with a stall-regulated method. *Journal of Mechanical Science and Technology*, *26*(1), 81-92.

Nakafuji, D. Y., Van Dam, C. P., Smith, R. L., & Collins, S. D. (2001). Active load control for airfoils using microtabs. *Journal of Solar Energy Engineering*,*123*(4), 282-289.

Richter, K., & Rosemann, H. (2002). Experimental investigation of trailing-edge devices at transonic speeds. *Aeronautical Journal*, *106*(1058), 185-193.

Schreck, S., Hand, M., & Fingersh, L. J. (2001). *NREL unsteady aerodynamics experiment in the NASA-Ames wind tunnel: a comparison of predictions to measurements*. Golden, CO, USA: National Renewable Energy Laboratory.

Shun, S., & Ahmed, N. A. (2012). Wind turbine performance improvements using active flow control techniques. *Procedia Engineering*, *49*, 83-91.

Tongchitpakdee, C., Benjanirat, S., & Sankar, L. N. (2006). Numerical studies of the effects of active and passive circulation enhancement concepts on wind turbine performance. *Journal of Solar Energy Engineering*, *128*(4), 432-444.

Van Dam, C. P., Chow, R., Zayas, J. R., & Berg, D. E. (2007). Computational investigations of small deploying tabs and flaps for aerodynamic load control. In *Journal of Physics: Conference Series* (Vol. 75, No. 1, p. 012027). IOP Publishing.

Wang, J. J., Li, Y. C., & Choi, K. S. (2008). Gurney flap—Lift enhancement, mechanisms and applications. *Progress in Aerospace Sciences*, *44*(1), 22-47.

Zayas, J. R., van Dam, C. P., Chow, R., Baker, J. P., & Mayda, E. A. (2006, February). Active aerodynamic load control for wind turbine blades. In*European Wind Energy Conference*.